PCCP

Accepted Manuscript

ROYAL SOCIETY OF CHEMISTRY

www.rsc.org/pccp

Journal Name

ARTICLE

Disaggregation-induced fluorescence enhancement of NIAD-4 for the optical imaging of amyloid-β fibrils

Received 00th January 20xx,
Accepted 00th January 20xx

DOI: 10.1039/x0xx00000x

www.rsc.org/

Francesca Peccati,[a] Jordi Hernando,*[a] Lluís Blancafort,[b] Xavier Solans,[a] and Mariona Sodupe*[a]

Alzheimer disease's main hallmark is the deposition of amyloid-β (Aβ) aggregates in the brain. An early diagnosis of the disease requires the fast and accurate detection of such aggregates *in vivo*. NIAD-4 is one of the most promising *in vivo* markers developed due to its high emission at λ > 600 nm and its ability to rapidly cross the blood-brain barrier (BBB) and target Aβ deposits. Furthermore, it shows a dramatic fluorescence enhancement upon binding to amyloid fibrils, which is essential for attaining a good imaging contrast. Aiming at establishing novel design concepts for the preparation of optimized optical probes, the current work rationalizes the excellent performance of NIAD-4 by using a pool of computational (TD-DFT and CASPT2 calculations, ab initio molecular dynamics and protein energy landscape exploration) and spectroscopic techniques. Unlike other markers operating as molecular rotors or polarity-sensitive dyes, we uncover herein that the high fluorescence imaging contrast observed upon NIAD-4 binding to amyloid fibrils results from reversible aggregation. NIAD-4 forms non-emissive assemblies in aqueous solution already at very low concentrations, which convert into the highly fluorescent monomeric species by diffusion into the hydrophobic voids of Aβ deposits. This result paves the way to exploit aggregation-induced processes as a new strategy towards advanced fluorescence markers for amyloid detection.

Introduction

Alzheimer's disease (AD), a progressive disorder of the central nervous system, is the most common form of neurodegenerative dementia. It shows several pathological hallmarks, including plaques caused by aggregation of the amyloid-β (Aβ) peptide into fibrils, tangles associated with the irregular phosphorylation of the tau protein, as well as inflammation and increased oxidative stress from the generation of reactive oxygen species (ROS).[1] According to the amyloid cascade hypothesis,[2] deposition of Aβ in the brain is a central event in the AD pathology. Thus, early detection of these deposits is crucial to monitor the progression of the neuropathologically derived disorders as well as the efficiency of novel drugs. Because of that, in the last years many efforts have been devoted to develop imaging probes both for nuclear modalities,[3–6] such as positron emission tomography (PET) or single photon emission computed tomography (SPECT), and for optical fluorescence imaging.[7–12]

Although positron emission tomography (PET) is the main technique used nowadays for *in vivo* detection of Aβ aggregates,[4,6] fluorescence imaging is a growing attractive alternative[7,11] due to its lower cost and safety.[13] Actually, several applications in animal models have already been reported. [7,10,11] For this application, however, optical markers must meet several tight requirements.[12,13]On the one hand, they must emit at λ > 650 nm in order to reduce biological photodamage, allow deeper tissue penetration and minimize autofluorescence background. In addition, fluorescent probes must be capable of crossing the blood brain barrier (BBB) and specifically target amyloid-β deposits. Finally, they should substantially modify their optical properties upon fibril binding, an essential condition to attain good contrast imaging.

Over the last years several different dyes such as Congo Red,[14] curcumin derivatives[11] or Thioflavin T (ThT)[16] have been proposed for staining amyloid fibrils. Among them, ThT has been one of the most widely used probes and is still employed for *in vitro* and *post mortem* histological analysis of AD brain. ThT behaves as a molecular rotor and gives rise to a non-fluorescent twisted internal charge transfer (TICT) excited state in solution via torsional motions around the single carbon-carbon bond connecting its two constituting aromatic moieties (Scheme 1).[16,17] This conformational flexibility is suppressed upon binding to the rigid channel-like motifs of the amyloid fibrils,[18] thus favoring the radiative relaxation of the excited state and a more than a 1000-fold increase in fluorescence quantum yield.[17] Unfortunately, ThT bears a positive charge and shows only very little permeation through the BBB.

NIAD-4 ({[5'-(*p*-hydroxyphenyl)-2,2'-bithienyl-5-yl]-methylidene}-propanedinitrile, Scheme 1), proposed by Nesterov *et. al.*,[10] is a promising alternative candidate to ThT, as it readily crosses the BBB, targets Aβ deposits, and exhibits very different photophysical properties when bound and unbound to Aβ fibrils; i.e., while NIAD-4 only shows trace fluorescence emission in aqueous solutions, it undergoes a dramatic fluorescence enhancement in the presence of Aβ aggregates (~400-fold).[10] Moreover, it has been assayed in living

[a] Departament de Química, Universitat Autònoma de Barcelona, 08193 Bellaterra, Spain. E-mail: Mariona.Sodupe@uab.cat, Jordi.Hernando@uab.cat
[b] Institut de Química Computacional i Catàlisi i Departament de Química, Campus Montilivi, Universitat de Girona, 17071, Girona, Spain

† Electronic Supplementary Information (ESI) available: [TDDFT absorption and emission wavelengths obtained at different levels of theory, HOMO and LUMO molecular orbitals, CASSCF, CASPT2 and MS-CASPT2 results, spin-orbit coupling calculations and spectroscopic experiments]. See DOI: 10.1039/x0xx00000x

mice and demonstrated to allow *in vivo* imaging of amyloid deposits. Although this behavior was tentatively ascribed to changes in polarity and rigidity of the surrounding medium upon fibril binding, a clear interpretation of NIAD-4 photophysics is yet to be given.

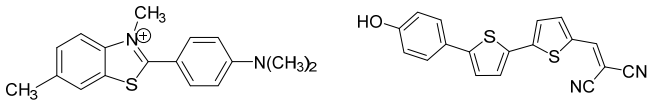

Thioflavin T (ThT) **NIAD-4**

Scheme 1 Structures of Thioflavin T and NIAD-4.

Understanding the photophysics of this and other dyes in solution and bound to amyloid fibrils is the starting point for the rational design of improved markers. This requires a good knowledge of their optical properties, as well as a deep comprehension of the affinity of these markers for amyloid fibrils. It should be noted that in the last years, a large amount of reliable structural information on amyloid fibril structures has been determined thanks to solid state nuclear magnetic resonance (NMR) and electron microscopy.[18,19] This information combined with computational simulation tools can offer relevant insights, at the molecular level, into the affinity of these markers for Aβ fibrils, as well as on the different photophysical properties in different environments.

In this work both computational and experimental techniques are combined to rationalize for the first time the environment dependent optical properties of NIAD-4. Results show that the main factor explaining the unusual high fluorescence enhancement of this dye is the disaggregation of non-emissive assemblies formed in water solution when interacting with Aβ fibrils. This enabled us to uncover the reversible aggregation of fluorophores as a potential novel strategy for the design of future optimized markers. Actually, despite the favorable features of NIAD-4 and other reported probes for amyloid detection,[12] their translation into clinical practice remains a challenge and further molecular improvements and technological evolutions are still required.

Methodology

Computational simulations

The ground and excited states of NIAD-4 were studied by means of Density Functional Theory (DFT) and Time-Dependent Density Functional Theory (TD-DFT) calculations with the Gaussian 09 package.[20] Several functionals and basis set were tested, since charge transfer transitions are known to be challenging for TDDFT.[22] Results showed that the CAM-B3LYP[23] functional in combination with the 6-31+G(d,p) basis set[24] is a cost effective level of theory that provides good results compared to experimental data (Table S1†). Moreover, solvation effects were taken into account using the PCM polarized continuum model,[25] within the non-equilibrium linear response (LR)-PCM solvation framework[25] for the absorption processes, and linear response equilibrium solvation for excited state optimizations, as implemented in Gaussian 09 package.[20] Moreover, for the most stable isomer of NIAD-4, we have carried out additional calculations using the state specific SS-PCM framework.[28,29] For the absorption process results show that the computed values differ by less than 9 nm, regardless of whether we use SS-PCM or LR-PCM. For the emission, however, while all approaches provide the same trend (the emission wavelength decreases with the polarity of the environment) larger variations (up to 60 nm), are observed, particularly for polar solvents (see Table S2† for details). Unexpectedly, best results compared to experiment are not obtained with SS-PCM but with LR-PCM, as already reported for other systems.[30] Moreover, in order to analyze possible deactivation pathways, we computed excitation energies for the low lying singlet and triplet states with TD-DFT(CAM-B3LYP). However, since previous studies showed that triplet excitation energies may be too low[31] with TD-DFT, we also performed calculations with the Tamm-Dancoff approximation (TDA), which has shown to significantly improve the triplet excitation energies, as well as with the CASSCF, CASPT2 and MS-CASPT2 methods,[32] including 12 electrons and 12 orbitals in the active space and considering 6 roots for the triplets and 12 for the singlets (Table S3†). Moreover, spin orbit coupling (SOC) was computed with MS-CASPT2 at different values of the relevant torsional angle of NIAD-4 (Table S4†). These post Hartree-Fock calculations were carried out using the Molcas 8 package[33] with an ANO-S basis set.[34]

Ab initio molecular dynamics (AIMD) simulations within the NVT ensemble at T= 300 K were also carried out with the CP2K package[33] to account for the influence of the flexibility of the molecule on the absorption wavelength.[35] These simulations were carried out using PBE-D3[36,37] in combination with the Goedecker-Teter-Hutter (GTH) pseudopotentials[38,39] and a DZVP basis sets.[40] The time step was set to 0.5 fs and the overall simulation time was 10 ps. For the simulation of the UV-Vis absorption spectra, we considered 40 regularly distributed snapshots for each isomer.

The binding site search and refinement of NIAD-4 interacting with fibrils models was performed with the PELE (Protein Energy Landscape Exploration) program, which allows performing an energy landscape exploration using a combination of a Monte Carlo stochastic approach and protein structure prediction algorithms.[41,42] Energies were evaluated with the OPLS force field[43] and the search was based on 150 trajectories.

Spectroscopic measurements

NIAD-4 was purchased from AOBIOUS Inc and used without further purification. All spectroscopic experiments were carried out in HPLC or spectroscopy quality solvents. Steady-state UV-vis absorption measurements were recorded on a HP 8453 spectrophotometer. Fluorescence emission spectra were measured in a custom-made spectrofluorometer, where a cw DPSS laser (λ_{exc} = 473 nm, SciTec) is used as excitation source and the emitted photons are detected in an ICCD camera (Andor) coupled to a spectrograph. Fluorescence quantum yields were determined relative to *N,N'*-bis(*sec*-butyl)-1,6,7,12-tetra-(4-*tert*-butylphenoxy)perylene-3,4:9,10-tetracarboxylic diimide in $CHCl_3$ (Φ_{fl} = 1.0).[44] Room temperature viscosities for the MeOH:glycerol mixtures used were taken from ref. [45]

Results and Discussion

Absorption and emission spectra of NIAD-4

As shown in Scheme 1, NIAD-4 has three single bonds that link the four different π-building blocks of the molecule together and allow

for conformational isomerism. DFT calculations indicate that there are three low-lying energy structures in the ground electronic state of this dye, none of which presents a planar geometry (Fig. 1 and Table 1). Excited state calculations at the geometry of these isomers indicate that the active transition ($S_0 \rightarrow S_1$) exhibits an important charge transfer character, as illustrated by the involved orbitals (see HOMO and LUMO in Figure S1†) and the computed dipole moments in the ground (12.8 D) and excited states (22.4 D) in aqueous solution. These three conformers lie very close in energy ($\Delta G < 5$ kJ mol^{-1}) and the rotational energy barriers that interconvert them are low ($\Delta G^{\ddagger} < 38$ kJ mol^{-1}). Therefore, all of them will contribute to the absorption spectrum of NIAD-4. The relative stabilities of the three conformers as well as the associated interconversion energy barriers are essentially not influenced by the dielectric constant of the medium, as illustrated in Table 1 for the two limiting cases.

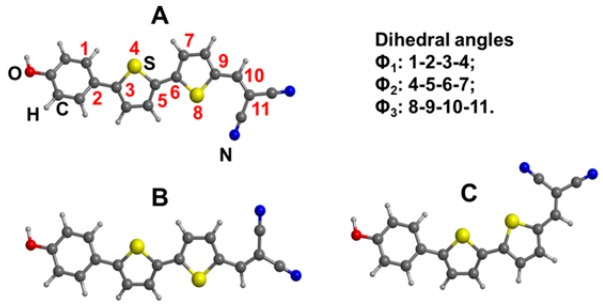

Fig.1 Geometries of the three most stable conformational isomers of NIAD-4 in the ground electronic state.

Table 1 Relative electronic and free energies and rotational barriers (kJ mol^{-1}) around dihedrals Φ_2 (A→C) and Φ_3 (A→B) with respect to isomer A in gas phase and in aqueous solution (in parentheses). The ground state equilibrium values of the dihedral angles Φ_1, Φ_2, Φ_3 are also reported. See Fig. 1 for labeling.

Geometry	A	B	C
ΔE (kJ mol^{-1})	0.0 (0.0)	1.2 (4.2)	3.4 (2.3)
ΔG (kJ mol^{-1})	0.0 (0.0)	1.5 (4.0)	4.4 (3.4)
Φ_1 (°)	33 (28)	33 (29)	33 (28)
Φ_2 (°)	-14 (-11)	-18 (-13)	155 (177)
Φ_3 (°)	1 (0)	-179 (-179)	1 (0)
Rotational barriers[a]		A → B	A→ C
$\Delta E^{\ddagger}$ (kJ mol^{-1})		37.5 (37.6)	14.0 (15.4)
$\Delta G^{\ddagger}$ (kJ mol^{-1})		38.6 (39.5)	19.2 (21.2)

[a] Rotational energy barriers (kJ mol-1) around dihedrals Φ_2 (**A→C**) and Φ_3 (**A→B**) with respect to isomer **A**.

In order to account for the influence of NIAD-4 flexibility on the absorption spectrum, we carried out *ab initio* molecular dynamics simulations at 300 K for each low-lying conformer (**A**, **B** and **C**), followed by TD-DFT (CAM-B3LYP) calculations of the excitation energy on 40 equally distributed snapshots sampled from each of the 10 ps-trajectory (120 total snapshots). This strategy has been shown to be particularly suitable for describing the absorption properties of complex flexible systems.[46–50] The histogram spectrum generated from vertical excitation energies (Fig 2b) shows an absorption band about 120 nm wide, where the broadening is due to its torsional flexibility. Noteworthy, the maximum absorption wavelength ($\lambda_{max,abs}$) is red-shifted by about 30 nm with respect to the vertical excitation energies directly computed with the CAM-B3LYP optimized conformers of NIAD-4. This is attributed to the fact that the molecular dynamics snapshots have been obtained with PBE-D3, which provides smaller torsional angles and thus, smaller excitation energies.

Table 2 and Fig. 2a-b compare the computed and experimental absorption spectral data for a number of solvents of increasing polarity. Calculations show that $\lambda_{max,abs}$ is very similar in all solvents (463-469 nm), thereby indicating that solvent polarity has a minor effect on the absorption spectrum of NIAD-4. The same trend is observed for the registered spectra in all organic solvents (470-480 nm), including a 1:2 mixture of *N*-methylformamide and MeOH, whose dielectric constant resembles that of water. In contrast, the absorption spectrum in water dramatically varies in shape and its $\lambda_{max,abs}$ blue-shifts to 429 nm, a striking different behavior which, according to TDDFT calculations and experimental data for the 1:2 mixture of *N*-methylformamide and MeOH, cannot be ascribed to solvent polarity effects on the energy of the electronic states of NIAD-4. This demonstrates that other effects should be responsible for the behavior of NIAD-4 in aqueous solution.

Table 2 Dependence of the optical properties of NIAD-4 on solvent polarity

Solvent	ε	$\lambda_{max,abs}$ [a] (nm)		$\lambda_{max,fl}$ [b] (nm)		Φ_{fl} (f) [c]
Diethyl ether	4.33	471	(463)	569	(573)	0.04 (1.67)
Dichloromethane	8.93	480	(470)	613	(598)	0.08 (1.67)
MeOH	32.7	475	(469)	651	(619)	0.14 (1.81)
H_2O	80.1	429	(469)	652	(625)	< 0.01 (1.82)
NMF:MeOH 1:2 [d]	84.8	478		651		0.15

[a] In parentheses theoretical values obtained from simulated spectra (Fig. 2). Computed vertical excitation energies (in nm) for the lowest energy conformer at the CAM-B3LYP optimized geometry are: 435 (diethyl ether), 440 (dichloromethane), 438 (MeOH) and 439 nm (H_2O). [b] In parentheses emission wavelength computed at the S_1 optimized geometry for the lowest energy isomer. [c] In parentheses computed oscillator strength for the emission process. [d] Mixture of *N*-methylformamide (NMF) and MeOH 1:2 v/v

Concerning the fluorescence emission wavelengths, both experimental and theoretical data show a larger dependence on solvent polarity. NIAD-4 emits at larger wavelengths when increasing solvent dielectric constant, the difference between diethyl ether (ε=4.33) and water (ε=80.1) being 83 nm (Table 2 and Fig. 2c). This is in agreement with the charge transfer character of the S_1 excited state and its larger dipole moment (see above), as already reported for similar push-pull oligothiophenes.[49] Moreover, while quantum yields and oscillator strengths are larger in organic solvents with increasing dielectric constant, the dye became essentially non-fluorescent ($\Phi_{fl} < 0.01$) in aqueous solution. This behavior is not predicted by the calculations, suggesting that it cannot be simply attributed to the effect of polarity on the oscillator strength of NIAD-4 radiative transitions. To rationalize this result, we addressed different possible deactivation pathways for the excited state of this dye.

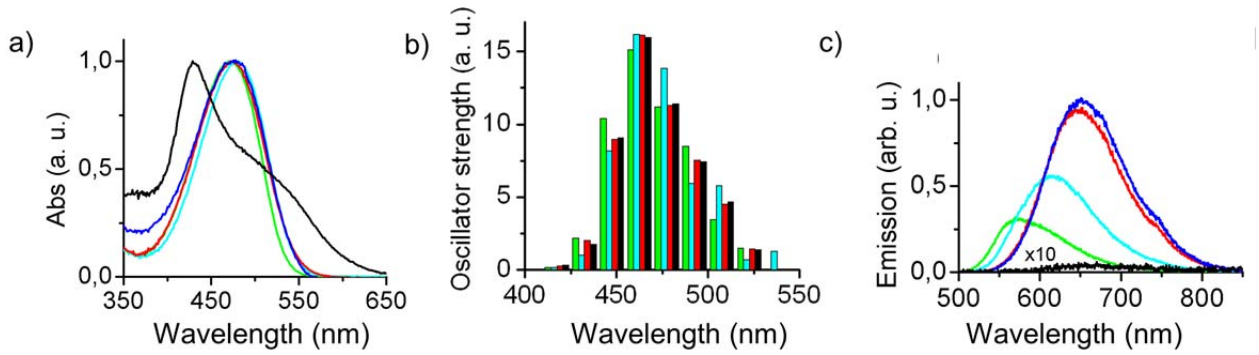

Fig. 2 (a) Absorption spectra of NIAD-4 (c_{NIAD-4} = 5 µM) in diethyl ether (green), dichloromethane (cyan), methanol (red), NMF:MeOH 1:2 mixture (blue) and water (black). All spectra are normalized to their absorption maximum. (b) Simulated absorption spectra of NIAD-4 in diethyl ether, dichloromethane, methanol and water from TDDFT CAM-B3LYP calculations on PBE-D3 molecular dynamics snapshots. (c) Fluorescence spectra of NIAD-4 (cNIAD-4 = 5 µM) in diethyl ether, dichloromethane, methanol, NMF:MeOH 1:2 mixture and water. Each fluorescence spectrum is normalized by the absorption at the excitation wavelength.

Non-radiative deactivation pathways

In view of the flexibility of NIAD-4 and based on other fluorescent markers such as ThT,[17] we first considered whether NIAD-4 behaves as a rotor and evolves to a non-radiative twisted internal charge transfer (TICT) excited state in environments with no spatial constraints, as originally suggested.[10] However, the optimized molecular structure of the dye in S_1 is fully planar instead of twisted (Fig. 3a) and displays a large oscillator strength. Similar planar structures are indeed predicted for the S_1 states of other polythiophenes,[51] thereby indicating that the bitiophene substituents in NIAD-4 have no influence on the geometry of the emitting state and that the photophysics of NIAD-4 should differ from that previously observed for ThT.[16–18] Moreover, the larger Φ_{fl} values determined in other non-viscous polar solvents such as MeOH and the NMF:MeOH mixture also suggest that evolution to a TICT excited state cannot explain the low fluorescence emission in aqueous solution. Consequently, this hypothesis is rejected herein for NIAD-4.

Intersystem crossing (ISC) between the emitting state and a triplet state close in energy may also be an effective non-radiative decay mechanism, as found for oligothiophenes in solution.[52] To explore this possibility, TDDFT calculations of S_1 and T_2, which is the triplet state closest in energy to S_1 and thus, the most prone to be involved in the ISC, were conducted at the optimized S_1 geometry and several fixed values of Φ_2 (see Fig. 1). Note that since previous studies showed that TDDFT triplet excitation energies may be too low[31] with TDDFT, the curves were corrected by adding a uniform shift corresponding to the difference between TDDFT and MS-CASPT2 values at the S_1 optimized geometry (Table S3†). Results show that T_2 state lies above S_1 regardless of the nature of the solvent. Moreover, S_1 presents a maximum and T_2 a minimum at Φ_2 = 90° in all cases. Thus, the lowest S_1/T_2 energy gap occurs at Φ_2 = 90°. Furthermore, for ISC to be effective, the spin-orbit coupling (SOC) must also be significant.

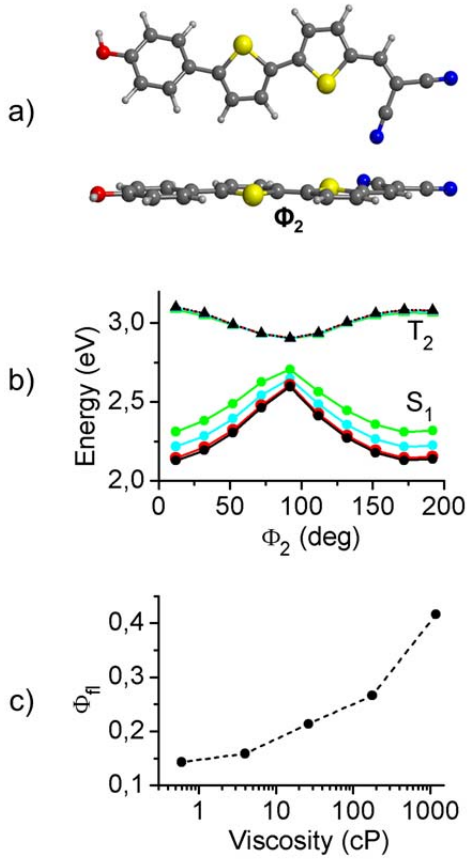

Fig. 3 (a) Geometry of the absolute energy minimum of the S_1 state of NIAD-4. (b) Dependence of the energy of the S_1 and T_2 states of NIAD-4 with dihedral angle Φ_2 (see Fig. 1) in diethyl ether (green), dichloromethane (cyan), methanol (red) and water (black). (c) Variation of the fluorescence quantum yield of NIAD-4 with the viscosity in glycerol:MeOH mixtures.

Computed SOC values in the gas phase are negligible for planar geometries and increase with Φ_2 (0.500 cm^{-1} for Φ_2=30˚; 2.017 cm^{-1} for Φ_2=40˚) (Table S3†). Both S_1/T_2 energy gap and SOC indicate that ISC will only be effective at highly twisted structures. This region is energetically accessible upon vertical absorption, providing a route for non-radiative relaxation of S_1.

Concerning the influence of solvent polarity, calculations show that while the energy of T_2 is essentially unaffected, S_1 is further stabilized when increasing the dielectric constant of the medium (Fig. 3b). This results in higher S_1/T_2 gaps and thus, in less effective ISC in solvents of increasing polarity, thus accounting (with the exception of water) for the increased Φ_{fl} values. Note that Φ_{fl} values cannot be justified by the computed oscillator strengths (see Table 2). The solvent polarity effects on ISC cannot explain the very low fluorescence in water and thus, the observed different optical properties of NIAD-4 in aqueous solution and upon interacting with Aβ fibrils.

The surrounding medium may affect the ability to achieve molecular geometries favorable for SOC and ISC, as well as the non-radiative deactivation through internal conversion. To explore this issue, we studied the effect of solvent viscosity in NIAD-4 optical response using MeOH:glycerol mixtures of rather similar dielectric constants (Fig. S2 and Table S5†). Noteworthy, a three-fold increase in Φ_{fl} was registered when switching the solvent from pure MeOH (η=0.594 cP) to pure glycerol (η=1182 cP) (Fig. 3c). This indicates a large contribution of conformational flexibility to non-radiative decay processes, which will result in a significant enhancement of fluorescence emission in rigid media (e.g. by increasing the rotational barriers in S_1 and, therefore, minimizing the non-radiative decay by ISC).[17] As such, larger fluorescence quantum yield values are expected for NIAD-4 upon fibril binding with respect to regular non-viscous organic solvents, where Φ_{fl} = 0.05-0.15. However, viscosity effects do not justify the distinct emissive behaviors found in MeOH (η=0.594 cP) and the NMF:MeOH 1:2 mixture (η~0.832 cP) with respect to H_2O (η=0.862 cP), and consequently, the dramatic fluorescence enhancement observed when transferring NIAD-4 molecules from aqueous solution into Aβ aggregates.

Aggregation effects

In view of the incapability to disclose the photophysical behavior of NIAD-4 in aqueous solution using purely solvent polarity and viscosity arguments, additional factors were investigated. Owing to the organic nature of NIAD-4 and its low solubility in water,[10] we considered the effect of dye aggregation on its optical behavior in aqueous media, a phenomenon already suggested to influence the photophysics of other amyloid probes.[53,54] Actually, co-facial self-assembly of fluorophores driven by π-stacking interactions has been long known to lead to the formation of aggregates displaying blue-shifted absorption and quenched emission,[55–57] as observed for NIAD-4 in aqueous solution. To verify this hypothesis, two different types of experiments were conducted: (i) concentration-dependent absorption spectra in water and water:MeOH mixtures (Fig. 4a and Fig. S3†); (ii) fluorescence excitation spectra in MeOH and aqueous solutions (Fig. 4b and Fig. S4†). This enabled us uncovering large spectral variations of the absorption of NIAD-4 in aqueous media with concentration, which only resembled that expected for the monomeric form of the dye ($\lambda_{max.abs}$ ~ 470 nm) at concentrations as low as 0.5 μM in water (and 5 μM in H_2O:MeOH 2:1 mixtures). Upon adding further amounts of NIAD-4, a new absorption band centered at 430 nm developed and became predominant in both cases, which can be attributed to the formation of non-emissive chromophore aggregates (the so-called H-dimers).[55] In addition, a weaker red-shifted band around 500 nm seems to develop upon aggregation as well, which may be attributed to the formation of cofacially-stacked assemblies with non-zero offset displacement between the monomeric units. In such a case, the optical transition to the lowest excitonic state would become weakly allowed.[55–57] Despite this, when registering the fluorescence excitation spectrum of such concentrated samples, we only detected very dim emission (Φ_{fl} < 0.01) that does not arise from the aggregates grown, but from the little amount of monomeric NIAD-4 species still remaining in solution. This is in contrast to the nearly identical absorption and fluorescence excitation spectra measured in MeOH, a good solvent for NIAD-4 where dye aggregation does not take place.

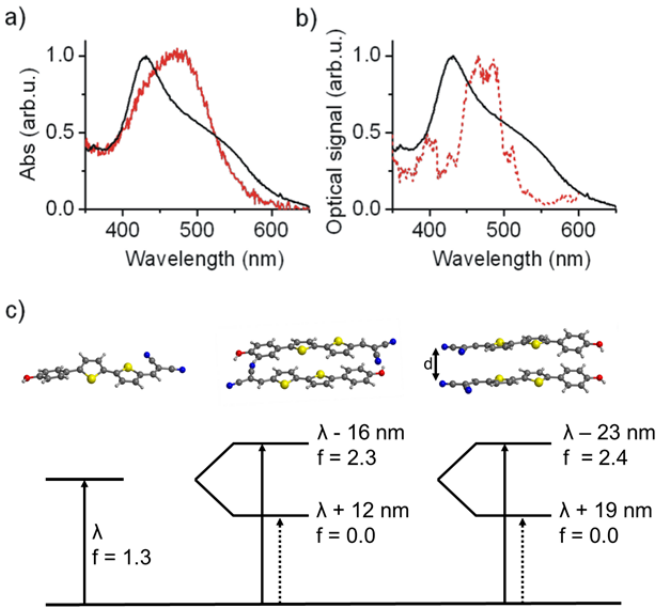

Fig. 4 (a) Absorption spectra of NIAD-4 in water at c= 0.5 μM (red) and 5 μM (black). (b) Comparison of the absorption (black) and fluorescence excitation (at λ_{em}=620 nm, red) spectra of NIAD-4 in H_2O (c_{NIAD-4} = 5 μM). (c) Computed optical properties for the non-centrosymentric and centrosymmetric co-facially stacked dimers of NIAD-4 at d = 4.2 Å in H_2O. Absorption maxima are related to those corresponding to the monomeric species.

To corroborate our experimental results, calculations were performed for the two possible stacked dimeric structures at different interchromophoric distances (d) ranging from 3.6 to 4.6 Å. For the sake of simplicity, we have only considered the centrosymmetric and non-centrosymmetric structures with zero offset displacement between the two units, keeping the geometry

of the isolated monomer. The results confirm the hypsochromic effect and the quenching of fluorescence predicted for this type of structures by the molecular exciton model[55] and demonstrated for several molecular aggregates.[56-57] That is, upon dimer formation the $S_0 \rightarrow S_2$ excitation transition blue-shifts with respect to that of the monomer ($\Delta\lambda \sim$ -15-20 nm) and carries a larger oscillator strength (f ~ 2), whereas the red-shifted $S_0 \rightarrow S_1$ transition ($\Delta\lambda \sim$ +15-30 nm) becomes optically inactive (f = 0). These results are illustrated in Fig. 4c for d = 4.2 Å.

In combination with the experimental data, they allow us to conclude that the aggregation of NIAD-4 in water is the main reason for the low fluorescence emission in aqueous solution, a process that might be reverted upon dye diffusion into the hydrophobic amyloid voids, resulting in a significant fluorescence enhancement. To explore this point, the binding process of NIAD-4 to Aβ fibrils was computationally investigated.

Binding sites of NIAD-4 in amyloid-*β* fibers

Three different models of Aβ fibrils were taken into account to study the interaction with NIAD-4 molecules (**I**, **II** and **III** in Fig. 5). Structures **I**[58] (PDB code 2LMN) and **II**[19] (PDB code 2LMQ) with two- and three-fold symmetry, respectively, were developed on fibrils grown *in vitro*, while three-fold symmetric structure **III** (PDB code 2M4J) is derived from Alzheimer's disease brain tissues.[19] A binding site search of all low-lying isomers of NIAD-4 was performed computationally for all these amyloid fiber models using the program PELE. [41,42] The preferred binding pose determined in each case is shown in Fig. 5. In all these structures, NIAD-4 is preferentially placed inside the fiber aggregate instead of adsorbed at its surface, and the dye-fibril interaction is dominated by dispersion forces, as it mainly involves hydrophobic aminoacids such as methionine and valine. Among the three models considered, the largest binding strength was determined for structure **I** (-338, -245 and -244 kJ mol^{-1} for **I**, **II** and **III**, respectively), where the dye molecule is accommodated at the junction of the two protofilaments, in the narrow channel defined by the two symmetric rows of M35 side chains. Binding pose for **II** involves the interaction of NIAD-4 with residues located at the corner of the internal cavity of the three-fold symmetry fiber, rich in glycine and M35 residues, whereas the binding in model **III** occurs with one of the three protofilaments, where it interacts with H13, E11, G38, and V39. Noteworthy, while the three-fold symmetry models **II** and **III** are able to accommodate all three conformers (**A**, **B** and **C**, see Fig 1) of NIAD-4, the two-fold symmetry model **I** shows a marked preference for conformers **A** and **B**. This is due to the nature of the channel formed in model **I**, which has an estimated elliptical cross section of around 6 Å x 11 Å that favors the binding of the two more linear conformers **A** and **B**. Although with different shapes, voids with similar small dimensions were found for the binding sites in the other fibril models. Moreover, in all the cases, none or minor geometrical distortion of the embedded NIAD-4 molecules was observed with respect to solution.

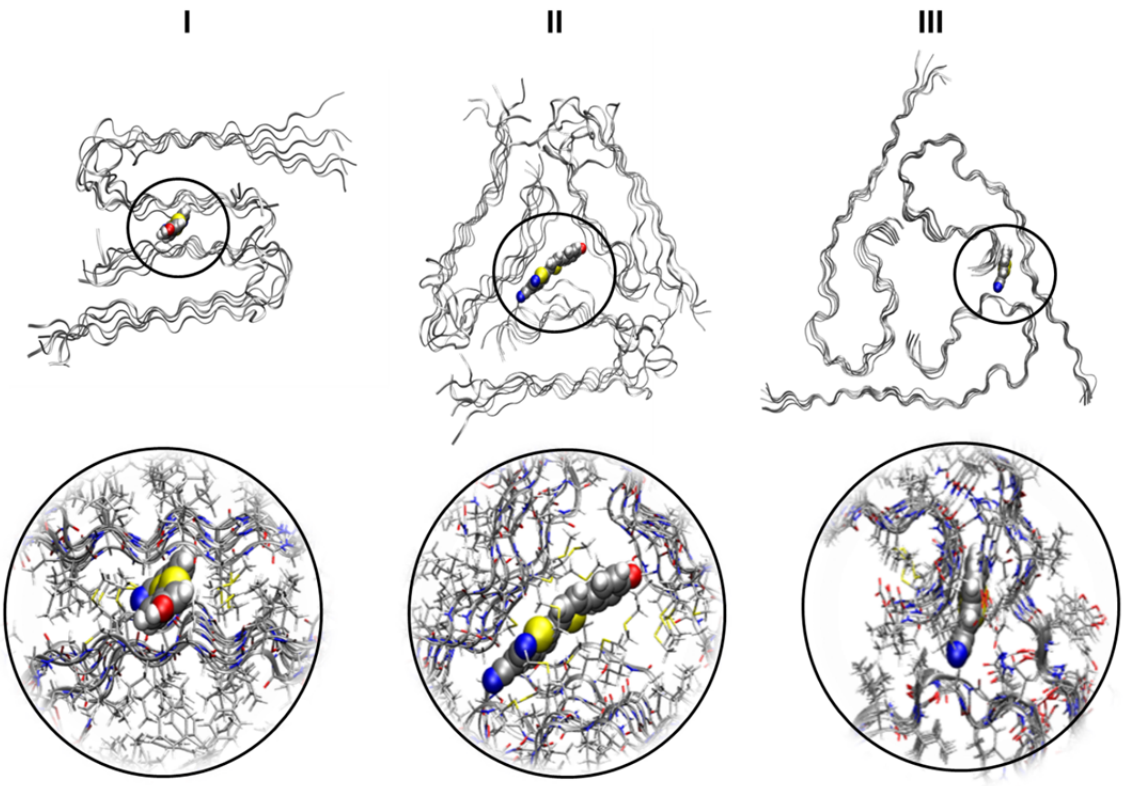

Fig. 5 Graphical representation of the binding poses of NIAD-4 on three different models of Aβ fibrils. The view is along the axis of the fiber.

Important implications derive from the small dimensions and hydrophobic nature of the preferred binding sites elucidated for structures **I-III**. First, and more notably, these sites can only accommodate the monomeric form of NIAD-4, which should result in chromophore disaggregation when diffusing from aqueous media into the Aβ deposits. Since small geometrical changes occur upon binding, the good emissive properties of non-aggregated NIAD-4 molecules in organic solvents are to be recovered once in the interior of the amyloid fibrils, thereby mostly accounting for the large fluorescence enhancement observed. On the other hand, the fluorescent behavior of bound NIAD-4 molecules must further benefit from the steric hindrance imparted by the surrounding fiber cavity, which should result in reduced conformational flexibility. Preliminary studies of dye rotational motion around Φ_2 revealed dramatic increases in energy up to ~ 100 kJ mol^{-1} even for torsional angles as small as 20^0, which we ascribe to the repulsive contacts between the fibers and the cyano groups of NIAD-4. This should therefore hinder the formation of the twisted geometries required for intersystem crossing ($\Phi_2 > 30^o$) as well as the conformational motions involved in internal conversion. As such, the rigidity of the surrounding amyloid matrix might additionally contribute to the increase in fluorescence intensity upon binding. In spite of this, our results unambiguously demonstrate that the primary cause for the high imaging contrast of Aβ deposits provided by NIAD-4 is dye disaggregation. Actually, the hydrophobic character of both NIAD-4 and the preferred binding sites of amyloid might be at the origin of the high selectivity experimentally observed for this marker to bind amyloid fibrils.

Conclusions

A combination of computational (TD-DFT and CASPT2 calculations, *ab initio* molecular dynamics and protein energy landscape exploration) and spectroscopic techniques has been used in this work to investigate the properties of NIAD-4, one of the first *in vivo* markers developed for amyloid fibril detection. In contrast to other similar probes, polarity and rigidity effects are not or minorly related to the efficiency of this dye. Instead, the primary cause for the excellent imaging contrast achieved with NIAD-4 arises from reversible chromophore aggregation, which converts the non-emissive assemblies formed in aqueous media into highly fluorescent monomers when diffusing into the narrow channels of Aβ deposits. This mechanism is associated to a ~400-fold emission enhancement upon fibril binding that largely exceeds the contrast found for other *in vivo* markers based on inhibition of molecular rotations or polarity-sensitive dyes. Therefore, our results pave the way for exploiting disaggregation as a novel strategy for the design of optimized fluorescence markers for amyloid detection.

Acknowledgements

The authors gratefully acknowledge financial support from MINECO (projects CTQ2012-30853, CTQ2011-26573 and CTQ2011-24847) and the Generalitat de Catalunya (projects 2014SGR-1202 and 2014SGR-482), and the use of computer time at the CESCA supercomputing center. MS acknowledges the Generalitat de Catalunya for the 2011 ICREA Academia award and XSM for a Professor Agregat Serra Húnter position.

Notes and references

1 D. Selkoe, *Physiol. Rev.*, 2001, **81**, 741–766.

2 J. Hardy and D. J. Selkoe, *Science*, 2002, **297**, 353–356.

3 C.-J. Chen, K. Bando, H. Ashino, K. Taguchi, H. Shiraishi, K. Shima, O. Fujimoto, C. Kitamura, S. Matsushima, K. Uchida, Y. Nakahara, H. Kasahara, T. Minamizawa, C. Jiang, M.-R. Zhang, M. Ono, M. Tokunaga, T. Suhara, M. Higuchi, K. Yamada and B. Ji, *J. Nucl. Med.*, 2015, **56**, 120–6.

4 C. a. Mathis, N. S. Mason, B. J. Lopresti and W. E. Klunk, *Semin. Nucl. Med.*, 2012, **42**, 423–432.

5 A. Kadir, A. Marutle, D. Gonzalez, M. Schöll, O. Almkvist, M. Mousavi, T. Mustafiz, T. Darreh-Shori, I. Nennesmo and A. Nordberg, *Brain*, 2011, **134**, 301–17.

6 V. L. Villemagne, W. E. Klunk, C. A. Mathis, C. C. Rowe, D. J. Brooks, B. T. Hyman, M. D. Ikonomovic, K. Ishii, C. R. Jack, W. J. Jagust, K. A. Johnson, R. A. Koeppe, V. J. Lowe, C. L. Masters, T. J. Montine, J. C. Morris, A. Nordberg, R. C. Petersen, E. M. Reiman, D. J. Selkoe, R. A. Sperling, K. Van Laere, M. W. Weiner and A. Drzezga, *Eur. J. Nucl. Med. Mol. Imaging*, 2012, **39**, 209–19.

7 M. Cui, M. Ono, H. Watanabe, H. Kimura, B. Liu and H. Saji, *J. Am. Chem. Soc.*, 2014, **136**, 3388–3394.

8 X. Zhang, S. Bloch, W. Akers and S. Achilefu, *Curr. Protoc. Cytom.*, 2012, **12**.

9 H. Fu, M. Cui, P. Tu, Z. Pan and B. Liu, *Chem. Commun. (Camb).*, 2014, **50**, 11875–8.

10 E. E. Nesterov, J. Skoch, B. T. Hyman, W. E. Klunk, B. J. Bacskai and T. M. Swager, *Angew. Chemie - Int. Ed.*, 2005, **44**, 5452–5456.

11 X. Zhang, Y. Tian, Z. Li, X. Tian, H. Sun, H. Liu, A. Moore and C. Ran, *J. Am. Chem. Soc.*, 2013, **135**, 16397–409.

12 M. Staderini, M. A. Martín, M. L. Bolognesi and J. C. Menéndez, *Chem. Soc. Rev.*, 2015, **44**, 1807–19.

13 V. Ntziachristos, *Annu. Rev.*, 2006, **8**, 1–33.

14 W. E. Klunk, R. F. Jacob and R. P. Mason, *Anal. Biochem.*, 1999, **266**, 66–76.

15 V. I. Stsiapura, A. A. Maskevich, V. A. Kuzmitsky, V. N. Uversky, I. M. Kuznetsova and K. K. Turoverov, *J. Phys. Chem. B*, 2008, **112**, 15893–15902.

16 N. Amdursky, Y. Erez and D. Huppert, *Acc. Chem. Res.*, 2012, **45**, 1548–57.

17 M. Biancalana and S. Koide, *Biochim. Biophys. Acta - Proteins Proteomics*, 2010, 1804, 1405–1412.

18 R. Tycko and R. B. Wickner, *Acc. Chem. Res.*, 2013, **46**, 1487–96.

19 J.-X. Lu, W. Qiang, W.-M. Yau, C. D. Schwieters, S. C. Meredith and R. Tycko, *Cell*, 2013, **154**, 1257–68.

20 M. J. Frisch, G. W. Trucks, H. B. Schlegel, G. E. Scuseria, M. A. Robb, J. R. Cheeseman, G. Scalmani, V. Barone, B. Mennucci, G. A. Petersson, H. Nakatsuji, M. Caricato, X. Li, H. P. Hratchian, A. F. Izmaylov, J. Bloino, G. Zheng, J. L. Sonnenberg, M. Hada, M. Ehara, K. Toyota, R. Fukuda, J. Hasegawa, M. Ishida, T. Nakajima, Y. Honda, O. Kitao, H. Nakai, T. Vreven, J. A. Montgomery Jr., J. E. Peralta, F. Ogliaro, M. Bearpark, J. J. Heyd, E. Brothers, K. N. Kudin, V. N. Staroverov, R. Kobayashi, J. Normand, K. Raghavachari, A. Rendell, J. C. Burant, S. S. Iyengar, J. Tomasi, M. Cossi, N. Rega, J. M. Millam, M. Klene, J. E. Knox, J. B. Cross, V. Bakken, C. Adamo, J. Jaramillo, R. Gomperts, R. E. Stratmann, O. Yazyev, A. J. Austin, R. Cammi, C. Pomelli, J. W. Ochterski, R. L. Martin, K. Morokuma, V. G. Zakrzewski, G. A. Voth, P. Salvador, J. J. Dannenberg, S. Dapprich, A. D. Daniels, Ö. Farkas, J. B. Foresman, J. V Ortiz, J. Cioslowski and D. J. Fox, *Gaussian Inc Wallingford CT*, 2009, 34, Wallingford CT.

21 D. Jacquemin, E. A. Perpète, I. Ciofini and C. Adamo, *Acc. Chem. Res.*, 2009, **42**, 326–34.

22 T. Yanai, D. P. Tew and N. C. Handy, *Chem. Phys. Lett.*, 2004, **393**, 51–57.

23 R. Ditchfield, W. J. Hehre and J. A. Pople, *J. Chem. Phys.*, 1971, **54**, 724.

24 S. Miertuš, E. Scrocco and J. Tomasi, *Chem. Phys.*, 1981, **55**, 117–129.

25 R. Cammi, S. Corni, B. Mennucci and J. Tomasi, *J. Chem. Phys.*, 2005, **122**.

26 R. Improta, V. Barone, G. Scalmani and M. J. Frisch, *J. Chem. Phys.*, 2006, **125**, 054103.

27 R. Improta, G. Scalmani, M. J. Frisch and V. Barone, *J. Chem. Phys.*, 2007, **127**.

28 D. Cheshmedzhieva, P. Ivanova, S. Stoyanov, D. Tasheva, M. Dimitrova, I. Ivanov and S. Ilieva, *Phys. Chem. Chem. Phys.*, 2011, **13**, 18530.

29 M. J. G. Peach, M. J. Williamson and D. J. Tozer, *J. Chem. Theory Comput.*, 2011, **7**, 3578–3585.

30 B. O. Roos, K. Andersson, M. P. Fulscher, P. A. Malmqvist, L. SerranoAndres, K. Pierloot and M. Merchan, in *Advances in Chemical Physics, Vol Xciii*, 1996, vol. 93, pp. 219–331.

31 F. Aquilante, T. B. Pedersen, V. Veryazov and R. Lindh, *Wiley Interdiscip. Rev. Comput. Mol. Sci.*, 2013, **3**, 143–149.

32 R. Pou-Amérigo, M. Merchán, I. Nebot-Gil, P. O. Widmark and B. O. Roos, *Theor. Chim. Acta*, 1995, **92**, 149–181.

33 J. VandeVondele, M. Krack, F. Mohamed, M. Parrinello, T. CHASSAING and J. Hutter, *Comput. Phys. Commun.*, 2005, **167**, 103–128.

34 J. Perdew, K. Burke and M. Ernzerhof, *Phys. Rev. Lett.*, 1996, **77**, 3865–3868.

35 S. Grimme, *J. Comput. Chem.*, 2006, **27**, 1787–1799.

36 C. Hartwigsen, S. Goedecker and J. Hutter, 1998, **58**.

37 S. Goedecker, M. Teter and J. Hutter, *Phys. Rev. B*, 1996, **54**, 1703–1710.

38 J. VandeVondele and J. Hutter, *J. Chem. Phys.*, 2007, **127**, 114105.

39 K. W. Borrelli, C. Benjamin and G. Victor, *J. Comput. Chem.*, 2010, **31**, 1224–1235.

40 K. W. Borrelli, A. Vitalis, R. Alcantara and V. Guallar, *J. Chem. Theory Comput.*, 2005, **1**, 1304–1311.

41 W. L. Jorgensen, D. S. Maxwell and J. Tirado-Rives, *J. Am. Chem. Soc.*, 1996, **118**, 11225–11236.

42 R. S. Sánchez, R. Gras-Charles, J. L. Bourdelande, G. Guirado and J. Hernando, *J. Phys. Chem. C*, 2012, **116**, 7164–7172.

43 J. A. Levitt, M. K. Kuimova, G. Yahioglu, P. H. Chung, K. Suhling and D. Phillips, *J. Phys. Chem. C*, 2009, **113**, 11634–11642.

44 M. Nadal-Ferret, R. Gelabert, M. Moreno and J. M. Lluch, *J. Chem. Theory Comput.*, 2013, **9**, 1731–1742.

45 E. Sanchez-Garcia, M. Doerr and W. Thiel, *J. Comput. Chem.*, 2009, n/a–n/a.

46 P. Imhof, *J. Chem. Theory Comput.*, 2012, **8**, 4828–4836.

47 C. M. Isborn, A. W. Götz, M. A. Clark, R. C. Walker and T. J. Martínez, *J. Chem. Theory Comput.*, 2012, **8**, 5092–5106.

48 N. De Mitri, S. Monti, G. Prampolini and V. Barone, *J. Chem. Theory Comput.*, 2013, **9**, 4507–4516.

49 M. M. Oliva, J. Casado, M. M. M. Raposo, A. M. C. Fonseca, H. Hartmann, V. Hernández and J. T. López Navarrete, *J. Org. Chem.*, 2006, **71**, 7509–20.

50 X.-Q. Ran, J.-K. Feng, Y.-L. Liu, A.-M. Ren, L.-Y. Zou and C.-C. Sun, *J. Phys. Chem. A*, 2008, **112**, 10904–11.

51 D. Beljonne, Z. Shuai, G. Pourtois and J. L. Bredas, *J. Phys. Chem. A*, 2001, **105**, 3899–3907.

52 H. LeVine, *Biochemistry*, 2005, **44**, 15937–43.

53 H. Benzeid, E. Mothes, E. M. Essassi, P. Faller and G. Pratviel, *Comptes Rendus Chim.*, 2012, **15**, 79–85.

54 M. Kasha, H. R. Rawls and M. Ashraf El-Bayoumi, *Pure Appl. Chem.*, 1965, 11, 371–392.

55 F. Würthner, S. Yao, T. Debaerdemaeker and R. Wortmann, *J. Am. Chem. Soc.*, 2002, **124**, 9431–9447.

56 J. Hernando, M. van der Schaaf, E. M. H. P. van Dijk, M. Sauer, M. F. García-Parajó and N. F. van Hulst, *J. Phys. Chem. A*, 2003, **107**, 43–52.

57 A. T. Petkova, W.-M. Yau and R. Tycko, *Biochemistry*, 2006, **45**, 498–512.

Table of Contents of

Disaggregation-induced fluorescence enhancement of NIAD-4 for the optical imaging of amyloid-β fibrils

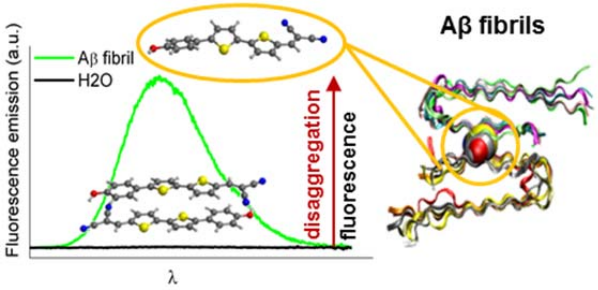

Fluorescence enhancement of NIAD-4 marker upon interacting with amyloid-β fibrils arises from the disaggregation of the oligomers that spontaneously form in aqueous solution.